Draft version June 1, 2023
Typeset using LaTeX **twocolumn** style in AASTeX62

Effects of partial ionization on magnetic flux emergence in the Sun.

Georgios Chouliaras,[1] P.Syntelis,[2] and V.Archontis[2,1]

[1]*School of Mathematics and Statistics, St. Andrews University, St. Andrews, KY16 9SS, UK*
[2]*Department of Physics, University of Ioannina, 45110, Ioannina, Greece*

(Accepted 26th May, 2023 ApJ)

ABSTRACT

We have performed 3-D numerical simulations to investigate the effect of partial ionization on the process of magnetic flux emergence. In our study, we have modified the single-fluid MHD equations to include the presence of neutrals and have performed two basic experiments: one that assumes a fully ionized plasma (FI case) and one that assumes a partially ionized plasma (PI case). We find that the PI case brings less dense plasma to and above the solar surface. Furthermore, we find that partial ionization alters the emerging magnetic field structure, leading to a different shape of the polarities in the emerged bipolar regions compared to the FI case. The amount of emerging flux into the solar atmosphere is larger in the PI case, which has the same initial plasma beta as the FI case, but a larger initial magnetic field strength. The expansion of the field above the photosphere occurs relatively earlier in the PI case, and we confirm that the inclusion of partial ionization reduces cooling due to adiabatic expansion. However, it does not appear to work as a heating mechanism for the atmospheric plasma. The performance of these experiments in three dimensions shows that PI does not prevent the formation of unstable magnetic structures, which erupt into the outer solar atmosphere.

Keywords: Sun: activity, Sun: interior, Sun: Magnetic fields, Magnetohydrodynamics, partial ionization (MHD), methods: numerical

1. INTRODUCTION

Magnetic flux emergence is a fundamental process in the Sun, which plays a key role on the driving and/or triggering of many dynamical phenomena, such as the formation of active regions, the onset of flares, jets, eruptions, etc. In the past, magnetic flux emergence has been studied in detail, via 3D MHD numerical simulations (e.g., Moreno-Insertis & Emonet 1996; Magara & Longcope 2001; Fan 2001; Manchester et al. 2004; Archontis et al. 2004) and references therein). The vast majority of these experiments have used a solar atmosphere assuming a fully ionized plasma. However, it is well known, that the solar photosphere and chromosphere are partially ionized, which brings the presence of electrons and neutrals in addition to the existence of ions in the atmospheric plasma.

Leake & Arber (2006) performed 2.5D MHD simulations of magnetic flux emergence including the presence of neutrals in the solar atmosphere. More precisely, they have used the generalised Ohms law for a fluid containing three different species given by Braginskii (1965) and they have neglected pressure and Hall term. They found that the rate of flux emergence in the solar atmosphere increased due to the effect of partial ionization. In addition, the emerging magnetic field appeared to be more diffusive. Another important result of this study was that, due to the perpendicular resistivity induced by the ion-neutral collisions, the currents that emerge to the corona were aligned with the field creating a force-free coronal field. We have to note that this model used a simple equation of state without the implementation of the ionization-recombination effect. Arber et al. (2007) extended the afore-mentioned model from 2.5D to 3D and they confirmed the results from the 2.5D simulations, highlighting that perpendicular resistivity successfully dissipates perpendicular current. Furthermore, this study showed that when partial ionization is considered, then less chromospheric material is lifted to the corona. Leake & Linton (2013) modified their previous 2.5D model by taking into account the ionization-recombination effect in the equation of state. They performed simulations of the emergence of magnetic flux tubes, with different radii and initial axial flux. They found

Corresponding author: Georgios Chouliaras
gc205@st-andrews.ac.uk

that the addition of ionization-recombination affects the rise speed of the tube's axis, which reaches smaller heights at the end of the simulations. Furthermore, this study showed that the energy in the sheared component of the magnetic field is reduced compared to the fully ionized case. In fact, it was reported that the tubes in the PI experiments lift up to 89 % less material than the fully ionized case. An interesting result of this study was that the implementation of the partial ionization to the equation of state led to the reduction of the free magnetic energy supplied to the corona. It was reported that the latter does not favour the formation of coronal structures that might become unstable and erupt.

In our study, we have extended the Leake & Linton (2013) model from 2.5-D to 3-D. Firstly, we confirm some of the results from their work. Secondly, we report new results as a consequence of the extension of this model to 3-D. Finally, we briefly discuss the recurrent eruptions, which occur after the emergence at the solar atmosphere. The structure of our paper is as follows: We present the model in chapter 2, then in chapter 3 we present the results and finally in chapter 4 we report our conclusions.

2. MODEL

2.1. *Equations*

We numerically solve the 3D time-dependent, compressible, resistive MHD equations in Cartesian geometry using the Lare3D code of Arber et al. (2001). We modify the equations to include the effects of partial ionization (neglecting Hall term). For that, we follow the 2.5D model of Leake & Linton (2013).

We assume populations of ions (i), neutrals (n) and electrons (e). Therefore, the total mass density (ρ), gas pressure (P) and specific energy (ϵ) are obtained by summing over the three species. For instance, $\rho = \sum_k m_k n_k$, where $k = i, e, n$ and m_k and n_k are the mass and number density of the species k.

The resulting MHD equations solved are:

$$\frac{D\rho}{Dt} = -\rho\nabla\cdot\mathbf{v}, \tag{1}$$

$$\rho\frac{D\mathbf{v}}{Dt} = -\nabla P + \mathbf{j}\times\mathbf{B} - g_0\hat{\mathbf{z}} + \mathbf{S}_{visc}, \tag{2}$$

$$\frac{D\mathbf{B}}{Dt} = -\mathbf{B}\left(\nabla\cdot\mathbf{v}\right) + \left(\mathbf{B}\cdot\nabla\right)\mathbf{v} - \nabla\times\left[\eta\mathbf{j}_\parallel + (\eta+\eta_\perp)\mathbf{j}_\perp\right], \tag{3}$$

$$\rho\frac{D\epsilon}{Dt} = -P\nabla\cdot\mathbf{v} + \eta j_\parallel^2 + (\eta+\eta_\perp)j_\perp^2 + Q_{visc}, \tag{4}$$

where $\mathbf{v}$, $\mathbf{B}$, ρ, P are namely the velocity vector, magnetic field vector, density and gas pressure. Gravity is $g_0 = 274$ m s^{-1}. Viscosity is added through $\mathbf{S}_{visc} = \frac{\partial\sigma_{ij}}{\partial x_j}\hat{\mathbf{e}}_i$ and $Q_{visc} = \varepsilon_{ij}\sigma_{ij}$, where $\sigma_{ij} = 2\nu\left(\varepsilon_{ij} - \frac{1}{3}\delta_{ij}\nabla\cdot\mathbf{v}\right)$ and $\varepsilon_{ij} = \frac{1}{2}\left(\frac{\partial v_i}{\partial x_j} + \frac{\partial v_j}{\partial x_i}\right)$, and $\nu = 622$ kg m^{-1} s^{-1} (10^{-2} in non-dimensional units). The current density is treated using its components parallel ($\mathbf{j}_\parallel$) and perpendicular ($\mathbf{j}_\perp$) to the magnetic field vector. These are defined as

$$\mathbf{j}_\parallel = \frac{(\mathbf{j}\cdot\mathbf{B})}{B^2} \quad \text{and} \quad \mathbf{j}_\perp = \frac{\mathbf{B}\times(\mathbf{j}\times\mathbf{B})}{B^2}, \tag{5}$$

where $\mathbf{j} = \frac{1}{\mu_0}\nabla\times\mathbf{B}$ is the full current density vector.

We do not calculate the uniform resistivity from the collision frequencies of electrons with ions and neutrals as Leake & Linton (2013). Instead, we use a constant uniform resistivity of $\eta = 4.6\ \Omega$ m (10^{-2} in non-dimensional units). That way, we focus only on the effects of the perpendicular resistivity term ($\eta_\perp$). The perpendicular resistivity due to the ambipolar diffusion of neutrals is given by

$$\eta_\perp = \frac{\xi_n B^2}{\alpha_n}, \tag{6}$$

where $\alpha_n = m_e n_e \nu'_{en} + m_i n_i \nu'_{in}$ is calculated using the effective collisional frequencies for electron-neutral collisions (ν'_{en}) and for ion-neutral collisions (ν'_{in}). These terms are calculated according to Leake et al. (2005). The neutral fraction (ξ_n) is defined as

$$\xi_n = \frac{n_n}{n_n + n_i}. \tag{7}$$

Just for clarity, we note here that the expressions and names used for the perpendicular resistivity vary in the literature. For instance, Leake & Linton (2013) refer to it as Pedersen resistivity ($\eta_p = \eta + \eta_\perp$), grouping the resistivity terms of the current density perpendicular to the field (Eq. 3, 4) in one term. Arber et al. (2007) refer to the perpendicular resistivity as Cowling resistivity ($\eta_c = \eta_\perp$), while Martínez-Sykora et al. (2012) refer to it as ambipolar diffusion resistivity ($\eta_{amb} = n_\perp$). Irrespective of the name used or the grouping of the terms, eventually, the terms used to describe the resistive effects in the induction and energy equation are the same. Effectively, there is little difference between Pedersen, Cowling and ambipolar diffusion resistivity.

We also solve the ideal gas law, which is

$$P = \frac{\rho k_B T}{\mu_m}, \quad \text{where} \quad \mu_m = \frac{m_i}{2 - \xi_n}. \tag{8}$$

For the reduced mass μ_m, we use $m_i = m_f m_p$, where m_p is the mass of proton and $m_f = 1.25$, k_B is Boltzmann constant.

For the specific internal energy equation, we take into account changes both to the temperature and to the ionization level,

$$\epsilon = \frac{k_B T}{\mu_m(\gamma - 1)} + (1 - \xi_n)\frac{X_i}{m_i}, \tag{9}$$

where $\gamma = 5/3$ and $X_i = 13.6$ eV is the first ionization energy of hydrogen. When performing simulations without the effects of partial ionization ($\xi_n = 0$), we omit the second term

of the equation and keep only the gas term to compare the results with previous simulations of fully ionized plasma.

We calculate ξ_n according to Leake & Linton (2013). Briefly, we use the Saha equation Saha (1921) below the photosphere (which is in local thermodynamic equilibrium) and the modified Saha equation Brown (1973) above the photosphere (which is not in local thermodynamic equilibrium), to derive the n_i^2/n_n ratio. Afterwards, the neutral fraction ξ_n is calculated.

The above set of equations is normalized using the photospheric values of density $\rho_{\rm u} = 1.67 \times 10^{-7}$ g cm^{-3}, length $H_{\rm u} = 180$ km and magnetic field strength $B_{\rm c} = 300$ G. Using the value of m_i mentioned before, we derive from these we get temperature $T_{\rm u} = 649$ K, velocity $v_{\rm u} = 2.1$ km s^{-1} and time $t_{\rm u} = 86.9$ s.

2.2. *Initial conditions*

We use a numerical domain the same as the one used in Syntelis et al. (2017). The computational domain has a physical size of 64.8^3Mm in a 420^3 uniform grid. The interior extends at -7.2 Mm$\leq z < 0$ Mm, the photospheric-chromospheric layer at 0 Mm$\leq z < 1.8$ Mm, the transition region at 1.8 Mm$\leq z < 3.2$ Mm and an isothermal corona at 3.2 Mm$\leq z < 57.6$ Mm. We assume periodic boundary conditions in the y direction. Open boundary conditions are used in the x direction and at the top of the numerical box. The bottom boundary is set to be closed. We place a cylindrical twisted flux tube (FT) $2.3Mm$ below photosphere.

We use two simulations in this study as mentioned above (FI and PI).

The background of both simulations is comprised by an adiabatically stratified solar interior (making the interior marginally stable to convection) and a stratified model atmosphere, both in hydrostatic equilibrium. We note that the reduced mass for the FI simulation is $\mu_m = m_i$ instead of $\mu_m = m_i/2$. That way we take into account the mass of the neutrals and get realistic coronal densities.

For both simulations, we assume the temperature of the atmosphere ($z > 0$) to follow a tangential temperature profile,

$$T(z) = T_{ph} + \frac{T_{cor} - T_{ph}}{2}\left(\tanh\frac{z - z_{cor}}{w_{tr}} + 1\right), \qquad (10)$$

where $T_{ph} = 6360$ K, $T_{cor} = 0.95$ MK, $z_{cor} = 2.52$ Mm and $w_{tr} = 0.18$ Mm. Having set this atmospheric temperature profile, we numerically solve the hydrostatic equation $dP/dz = -gz$ to derive the density of the atmosphere. We get a photospheric density of $\rho_{ph} = 1.67 \times 10^{-4}$ kg m^{-3}. For PI, we also calculate the neutral fraction ξ_n of the resulting T and ρ profiles.

To setup the initial stratification below the photosphere ($z < 0$), we require the vertical temperature gradient, assuming that a plasma element moves adiabatically. That is estimated using energy Eq. 9. For the FI simulation ($\xi_n = 0$) we omit the second term of Eq. 9, which simplifies the equation significantly. From that equation, the temperature profile for FI is:

$$\left(\frac{dT}{dz}\right)_a = -\frac{\mu_m g}{k_B}\frac{\gamma - 1}{\gamma}. \qquad (11)$$

This equation is solved analytically and then the density is calculated by solving numerically the hydrostatic equation. The boundary conditions are T_{ph} and ρ_{ph}. This stratification is used in all FI flux emergence simulations (e.g. Fan 2001; Manchester et al. 2004; Archontis et al. 2004; Moreno-Insertis et al. 2008; Toriumi & Yokoyama 2011; Leake et al. 2013; Syntelis et al. 2015).

However, in PI, the full Eq. 9 is needed in order to derive the temperature profile of the solar interior. Otherwise, the PI interior will not be adiabatically and convectively stable. Taking into account the full Eq. 9, Leake & Linton (2013) showed that the temperature profile for the solar interior becomes:

$$\left(\frac{dT}{dz}\right)_a = -\frac{\mu_m g}{k_B}\frac{\gamma - 1}{\gamma}\left(\frac{1 + \theta^{\frac{\zeta(1-\zeta)}{2}}}{\frac{\gamma}{\gamma-1} + \theta^{2\frac{\zeta(1-\zeta)}{2}}}\right), \qquad (12)$$

where

$$\theta = \frac{\gamma}{\gamma - 1} + \frac{X_i}{k_B T}, \quad \text{and} \quad \zeta = 1 - \xi_n. \qquad (13)$$

The method to solve this equation is described in Leake & Linton (2013). Briefly, we initially set $\zeta = 1$ (i.e. assume the plasma to be FI) and use as boundary conditions T_{ph} and ρ_{ph}. We use a 4th order Runge-Kutta scheme to solve Eq. 12 for $z < 0$ and then find the density by numerically solving the hydrostatic equation. Using the Saha equation, we calculate for the current T and ρ a new ionization fraction, ξ_n, and then the new ζ and θ. Then, we iterate these steps, until ζ converges for a set of T, ρ in the interior.

The resulting temperature, density and neutral fraction of the stratified interior and atmosphere is shown in Fig. 1. We overplot the same parameters from the model atmosphere C7 of Avrett & Loeser (2008) for comparison.

Inside the interior, we place a horizontal cylindrical twisted flux tube along the y-axis. The magnetic field of the flux tube is defined as

$$B_y = B_0 \exp(-r^2/R^2), \qquad (14)$$

$$B_\phi = \alpha r B_y, \qquad (15)$$

where $R = 450$ km is a measure of the FT's radius, r is the radial distance from the FT's axis and $\alpha/2\pi$ is the twist per unit of length. We set $\alpha = 0.4$ (0.0023 km^{-1}), which makes the flux tube highly twisted but kink stable.

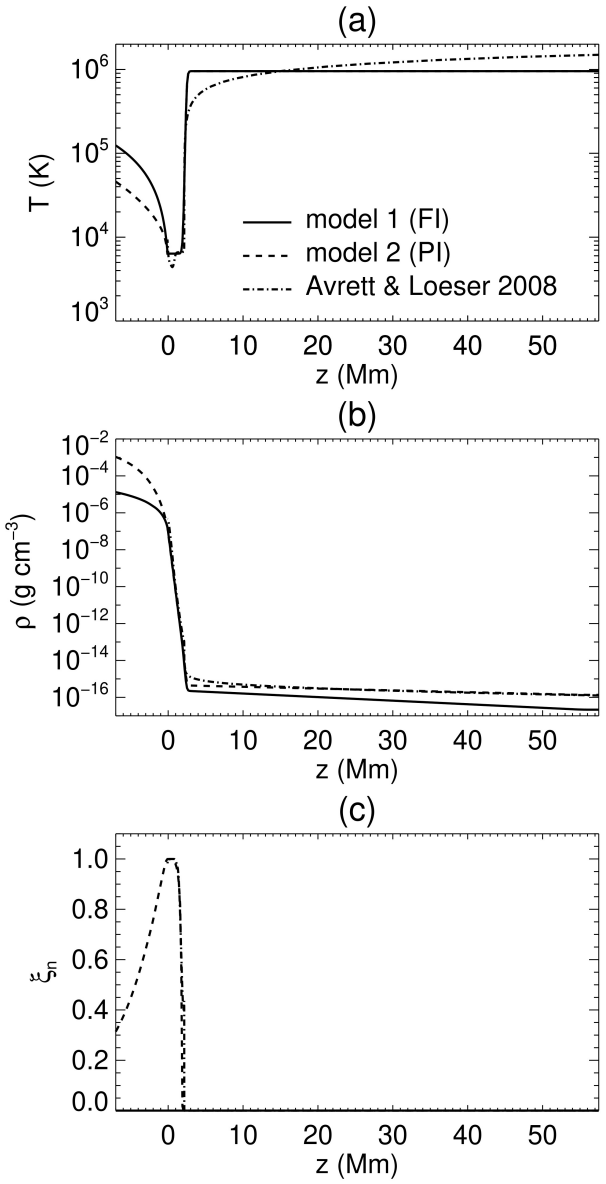

Figure 1. The (a) temperature stratification, (b) density stratification and (c) the neutral fraction of the solar interior and the atmosphere of the simulations. The solid line is FI (solid) and the dashed line is PI (dashed). Over plotted with a dashed-dot line is model C7 of Avrett & Loeser (2008) for comparison.

For FI, we set the magnetic field's strength to $B_0 = 3150$ G ($\beta = 18.4$), same to Syntelis et al. (2017). That way, the FI simulation is similar to the one described in detail in Syntelis et al. (2017) and direct comparisons can be made. Notice in Fig. 1 that the FI and PI background stratifications have different densities and temperatures in the interior, as it results from solving two different equations. For PI, we, therefore, do not use the same B_0 as FI, but the same β. That results to $B_0 = 7882$ G for PI.

To make the flux tube emerge, we change the density profile inside the flux tube. For FI, we use the usual method (e.g. Fan 2001). The background solar interior has a pressure, temperature and density profile of P_0, T_0 and ρ_0. By adding the flux tube, we add an additional pressure excess due to the magnetic field. Firstly, we require this pressure excess to be in radial force equilibrium $(dP_{exc}/dr) = (\mathbf{j}\times\mathbf{B})\hat{\mathbf{e}}_r$, finding the equation of P_{exc} to be (see Murray et al. 2006, for details):

$$P_{exc} = \frac{1}{2\mu}\left[\alpha^2\left(\frac{R^2}{2} - r^2\right) - 1\right]B_y^2 \tag{16}$$

Then, we require the flux tube to be in pressure equilibrium. The gas pressure in the interior of the tube, P_i, becomes $P_i = P_0 - P_{exc}$. Because inside the solar interior the isotropic thermal conduction is large, we expect the magnetized plasma to be in thermal equilibrium with the background non-magnetized plasma. We therefore set the flux tube to be in thermal equilibrium with the background ($T_i = T_0$). That leads to a density deficit ($\Delta\rho = \rho_i - \rho_0$) in the interior of the flux tube of $\Delta\rho = -\rho_0 P_{exc}/P_0$ that makes the flux tube buoyant. To avoid emerging the whole length of the flux tube, we reduce the density deficit towards the flanks of the flux tube by

$$\Delta\rho = -\rho_0 \frac{P_{exc}}{P_0} e^{-y^2/\lambda^2}, \tag{17}$$

where λ is thus a measure of the length of the buoyant part of the flux tube. The above ensures that the middle part of the flux tube will be buoyant, while the flanks will not. Thus the flux tube will adopt an Ω-loop shape. We use $\lambda = 0.9$ Mm.

For PI we need to follow the same steps, but also take into account that changes in ρ_i result in changes in the neutral fraction and therefore the reduced mass in the interior of the tube. P_{exc} will be the same. By setting $P_i = P_0 - P_{exc}$ and $T_i = T_0$, we get when the flux tube is in pressure balance and in thermal equilibrium with the background, the density in the interior of the flux tube is:

$$\rho_{i,teq} = \rho_0 \frac{\mu_{mi}}{\mu_{m0}}\left(1 - P_{exc}/P_0\right), \tag{18}$$

where μ_{mi} and μ_{m0} are the reduced mass of the interior of the flux tube and of the non-magnetized background. To make the flux tube adopt an Ω-loop shape as before, we use a function that sets the density at the middle part of the flux tube to $\rho_i = \rho_{i,teq}$ and at the flanks to $\rho_i = \rho_0$:

$$\Delta\rho = -\rho_0\left[1 - \frac{\mu_{mi}}{\mu_{m0}}\left(1 - P_{exc}/P_0\right)\right]e^{-y^2/\lambda^2}. \tag{19}$$

Indeed, notice that for $y = 0$, $\rho_i = \rho_{i,teq}$ and that for $y \gg \lambda$, $\rho_i = \rho_0$. Also, for $\mu_{mi} = \mu_{m0}$ (i.e. non PI effects), we recover Eq. 17.

To calculate ρ_i and μ_i , we numerically solve Eq. 19 in the following manner:

1. First, P_{exc} is calculated and $P_i = P_0 - P_{exc}$ is set.
2. Then, μ_{m0} of the background is found.
3. An initial guess for μ_{mi} is assumed to be $\mu_{mi} = \mu_{m0}$.
4. Then, ρ_i is calculated from Eq. 19.
5. The internal energy ϵ_i is calculated from Eq. 9. Then, the temperature T_i is calculated from Eq. 8
6. Based on the current values of temperature and density, the new ξ_{ni} and μ_{mi} are computed.
7. Steps 4-6 are repeated until ξ_{ni} converges to a value.

Using the above method, we derive the temperature, specific energy, density and gas pressure profile of the flux tube and the corresponding neutral fraction of the magnetized plasma.

3. RESULTS

3.1. *Magnetic flux emergence at the solar interior*

To study the emergence of magnetic flux below the photosphere, we first follow the rise of the centre and the apex of the tube in both simulations. We define the centre of the tube as the location at the vertical xz-midplane, where B_y is maximum and B_x changes its sign across the tube, along height. For simplicity, we define the apex of the tube to be at the outskirts of the magnetic field, where the magnetic field strength decreases to a value of about $0.001 \times B_0$. Figure 2 shows the time evolution of the emergence in both simulations.

We find that, in both simulations, the tube's axis emerges in a similar fashion until about $t = 25$ minutes (figure 2). However, after $t = 25$ minutes, we find that the two flux tubes emerge in a different manner. The axis of the tube in FI continues to rise until it reaches the photosphere, while in the other case the axis of the tube stays at around $2Mm$ below the photosphere until the end of the simulation. A similar result was reported by Leake & Linton (2013), who suggested that the reason for this difference is the ionization-recombination effect, induced by the ion-neutral collisions, at the upper part of the solar interior. In Figure 2, we also find that the expansion of the magnetic field above the photosphere occurs earlier in the PI simulation. This is because, the inclusion of the ion-neutral collisions and the increased dissipation allows the magnetic field to slip through the plasma during emergence and, thus, it doesn't carry within it so dense plasma as in the FI case. Thus, the apex of the field is less heavy in the PI case and it can expand earlier.

A similar effect is apparent also below the photosphere. Figure 3 and Figure 4 show the emergence of the magnetic flux tube in the solar interior for the two cases. The contours show the cross-section of the tube at the vertical xz-midplane and they correspond to values of B_y greater than $3 \times 10^{-3} T$. In the FI case (figure 3), the emergence of the field follows a typical behaviour, as this has been shown in many similar magnetic flux emergence experiments in the past. Namely, the tube rises vertically upwards and when it reaches the photosphere, it slows down and expands horizontally before it becomes unstable and emerges above the photosphere. In the PI case (figure 4) the shape of the cross-section of the tube is different, especially its top part and while it approaches the photosphere. We find that it is less flat and it does not expand horizontally as in the FI case, adopting an overall spindle-like shape. For instance, at $t = 22$, $t = 33$ and $t = 43$ minutes, we observe a more vertical than horizontal stretching/expansion. We anticipate that it is the perpendicular resistivity that dissipates the cross-field currents and this permits the magnetic field to "slip" through the plasma, giving this characteristic shape to the emerging field. As a consequence, the emerging bipolar region at the photosphere adopts a different shape as we show in the next section.

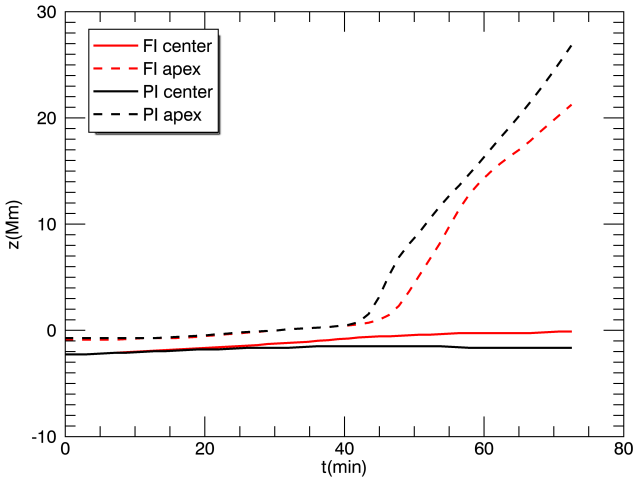

Figure 2. Height-time profile of the apex and center of the tubes in both simulations.

3.2. *Magnetic flux emergence at the photosphere*

Figure 5 shows the vertical component of the magnetic field at the photosphere at different times. In general, the time evolution shows the typical behaviour of an emerging bipolar region. First, the two opposite polarities appear along the x-axis, almost perpendicular to the direction of the original axis of the tube due to the strong twist and then they move apart along the y-axis. In between them, a strong polarity inversion line (PIL) is formed. There are some profound differences in the appearance and evolution of the emerging region in the two cases. In the PI case, the two polarities appear to adopt a more circular and compact shape. In a qualitative manner, this result is consistent with the shape of the emerging cross-section of the tube in Figure 5 (first row), where the magnetic field contours appear more vertical at the intersection with

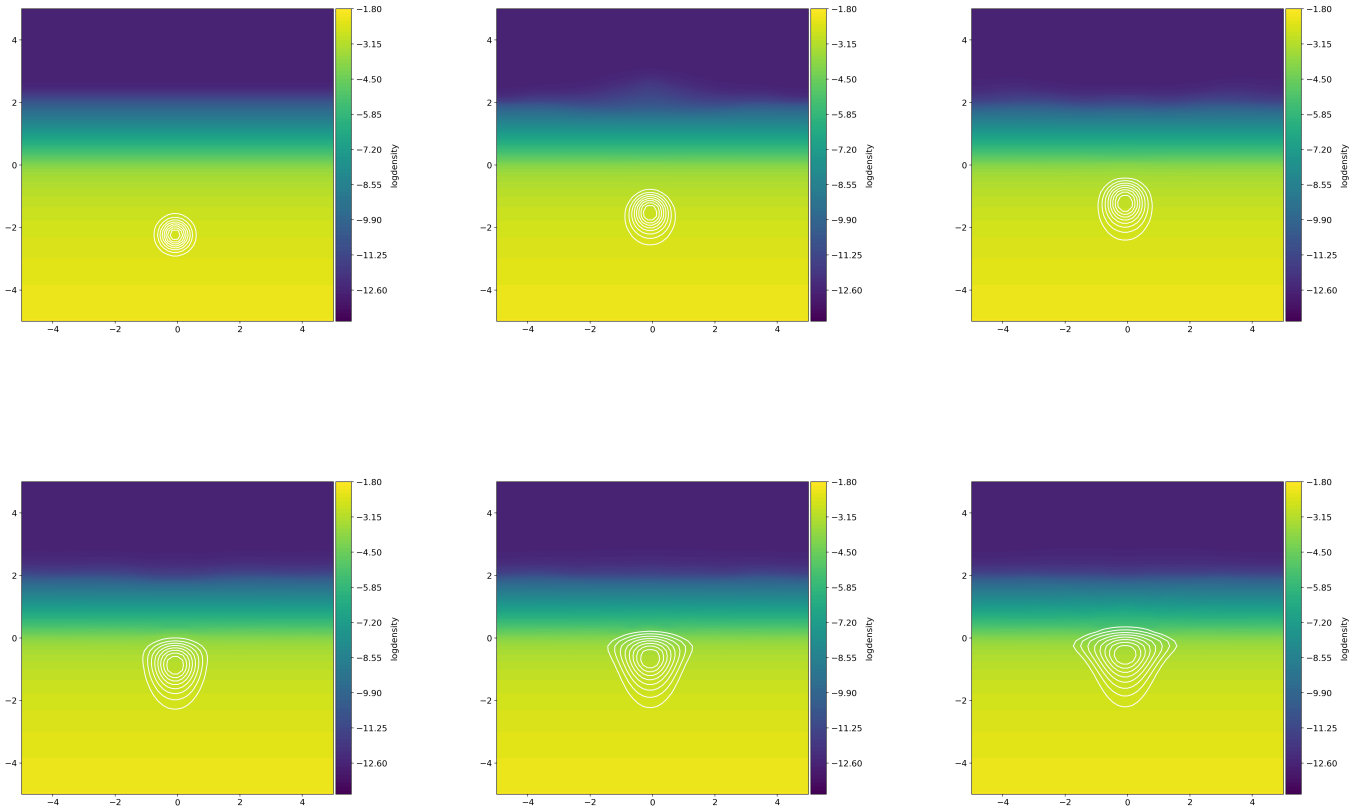

Figure 3. The evolution of By on xz plane on the FI simulation from up left to bottom right at t=0,22,29,36,40,43 minutes.

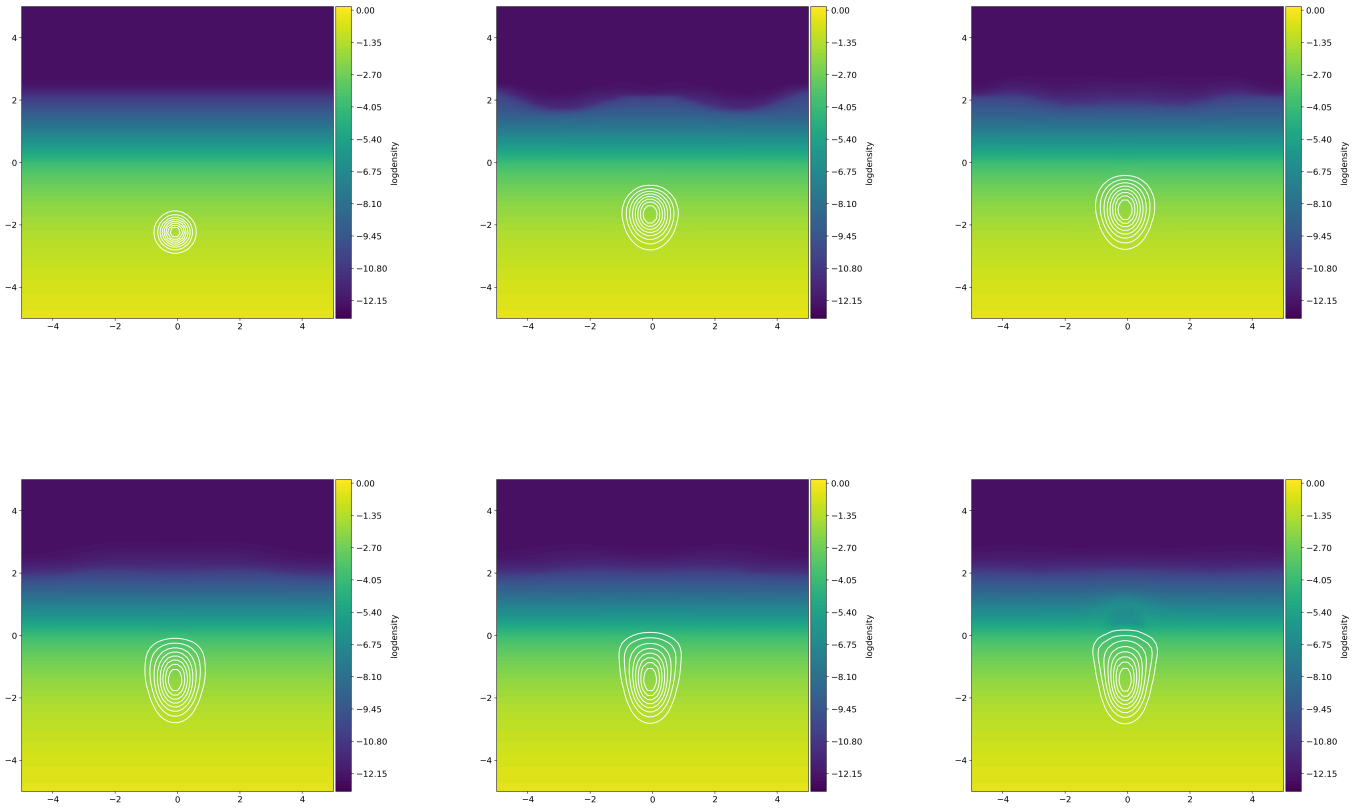

Figure 4. The evolution of By on xz plane on the PI simulation from up left to bottom right at t=0,22,29,36,40,43 minutes.

the photosphere in the PI case. Also, Figure 5 (second row) shows that in the FI case the magnetic tails, on the two sides of the PIL, are more noticeable. To understand better the reason(s) for the manifestation of these differences we study the evolution of the individual components of the magnetic field at the photosphere. More precisely, in Figure 6, we plot the maximum values of the components at the x=y=0 and at the base of the photosphere. We normalize them with the maximum value of the initial total magnetic field. Firstly, we notice that, overall, a larger percentage of the magnetic field components emerge to the photosphere in the FI case. Secondly, we find that in the PI case, the dominant component is Bz, which explains the more profound appearance of the two polarities at the photosphere in Figure 5 (first row). In the FI case the dominant component is the axial component By, which is consistent with the height-time profile of the axis of the tube in Figure 2. The second strongest component in the FI case is the azimuthal component of the magnetic field, while it is the weakest in the PI case. This explains why the magnetic tails are more noticeable in the FI case.

3.3. *Flux and energy evolution*

To study the relative importance between the emergence and shearing, we follow the time evolution of the Poynting flux at z=1.2Mm . More precisely, we have split the Poynting flux into two terms, the "emergence" and the "shear" term as shown below:

$$S_{xy}emergence = +\frac{1}{4\pi}\int_x\int_y v_z(B_x^2 + B_y^2)dxdy \qquad (20)$$

$$S_{xy}shear = -\frac{1}{4\pi}\int_x\int_y (v_xB_x + v_yB_y)B_zdxdy \qquad (21)$$

Figure 7 (8) shows the time evolution of the two terms in the FI (PI) case. Figure 9 shows the difference between the shear and the emergence term. Initially, in both cases (Figures 7 and 8), the emergence term is larger than the shear term, which is reasonable, since the intense shearing starts after the bipolar region emerges at the photosphere. Eventually, the shear term becomes larger than the emergence term and it becomes the dominant term during the evolution of the system. After t= 80min, the oscillatory behaviour is due to eruptions. The formation and evolution of the eruptive structures will be discussed in a follow up paper. The difference between the two terms is larger in the PI case (9). However,

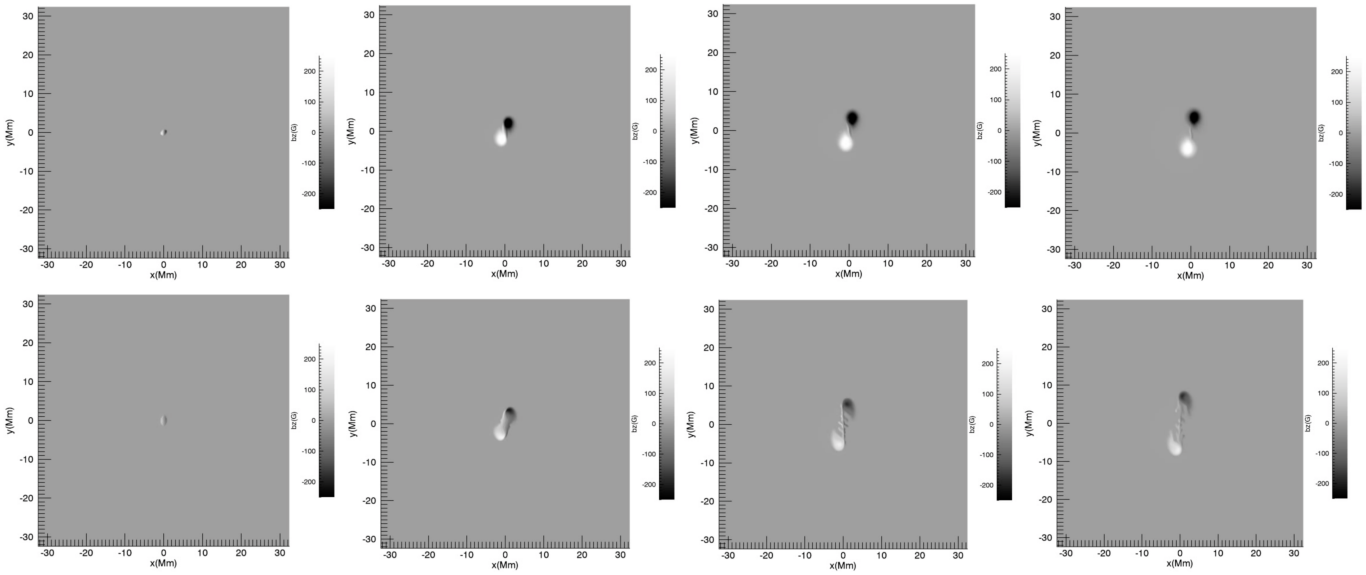

Figure 5. The evolution of bipolar region on PI simulation(first row) and FI simulation (second row) from left to right 43,72,115 and 159 minutes.

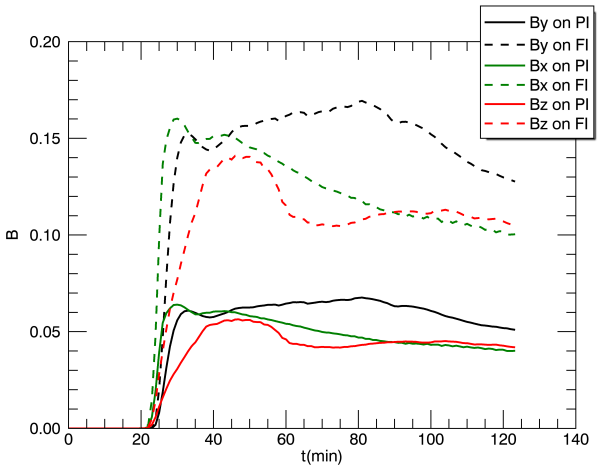

Figure 6. Time evolution of the normalized B components at the base of the photosphere.

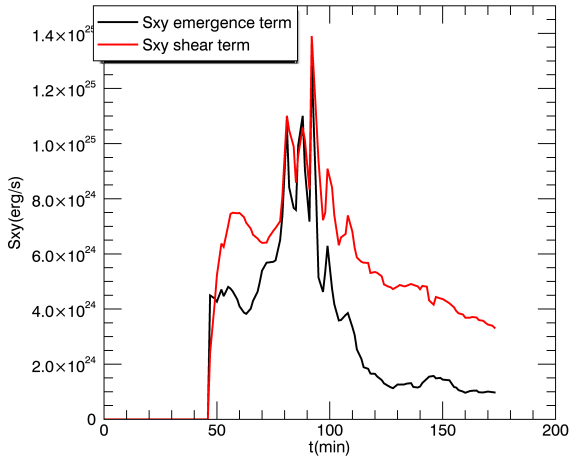

Figure 7. Emergence and shear term of Poynting flux on FI simulation at the mid-photosphere.

in the FI case with the same initial value for B, the difference of the two terms is even larger. The latter indicates that the inclusion of the partial ionization alone does not determine solely the amount of energy and/or flux, which is transferred at the photosphere and above an emerging bipolar region.

We have also computed the normalized in plane flux as follows:

$$\frac{F_{xz}}{F_{xz_0}} = \frac{\int_{z>1.2Mm}\int_x B_y dxdz}{\int_z\int_x B_{y_0} dxdz} \tag{22}$$

where, By_0 is the axial component of the magnetic field inside the flux tube at t=0. The result is shown in figure 10. Initially, for t <= 53min, the in plane flux is larger for the PI case because the tube emerges and expands above the photosphere earlier. Eventually, it is the FI case where the in plane flux becomes bigger during the time evolution of the system. Therefore, it seems that a larger percentage of axial field (By) is transferred above the photospher in the FI case. We have also computed the unsigned normalized in plane vertical flux by using the following formula:

$$\frac{F_{xy}}{F_{xy_0}} = \frac{\int_x\int_y |B_z| dxdy}{\int_x\int_y |B_{z_0}| dxdy} \tag{23}$$

We normalized it over the total initial in-plane vertical flux, we used the whole domain for the x and y-axis, while z is equal to 1.2 Mm above the photosphere, this is on figure 11. In both cases, there is an initial rapid increase in the flux,

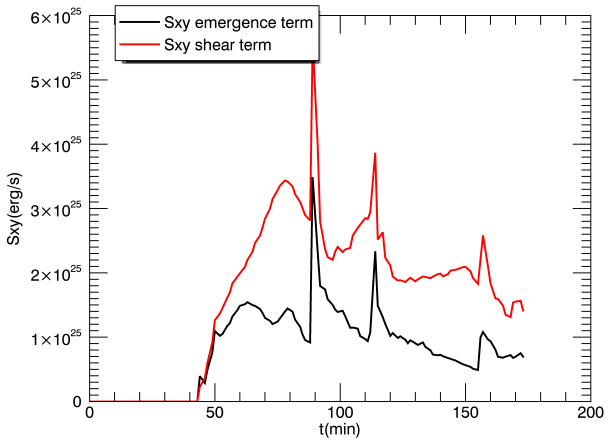

Figure 8. Emergence and shear term of Poynting flux on PI simulation at the mid-photosphere.

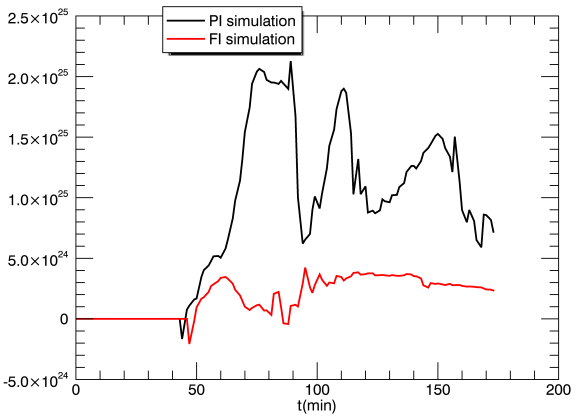

Figure 9. The difference between the shear and emergence terms of the Poynting flux.

which is due to the initial emergence of the magnetic flux tube at this height. This is followed by a slow increase and then saturation of the vertical flux, due to the fact that the available flux for emerging at this height has reached its limit. Overall, we find that the maximum value of the vertical flux above photosphere is similar in both cases (a bit larger in the FI case) and certainly the inclusion of PI does not lead to the emergence of more vertical flux at the solar atmosphere.

We have also computed an estimate of how much axial field energy(i.e due to the axial field component By) from the total magnetic energy, is transferred to the solar atmosphere. To do this, we calculate:

$$E_{axial} = \frac{\int_x \int_{z>0.36} B_y^2 dxdz}{\int_x \int_{z>0.36} |B|^2 dxdz} \quad (24)$$

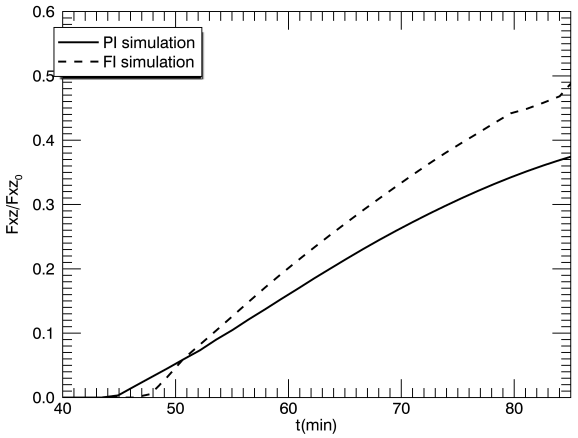

Figure 10. Emerged normalized in plane flux above z=1.2Mm.

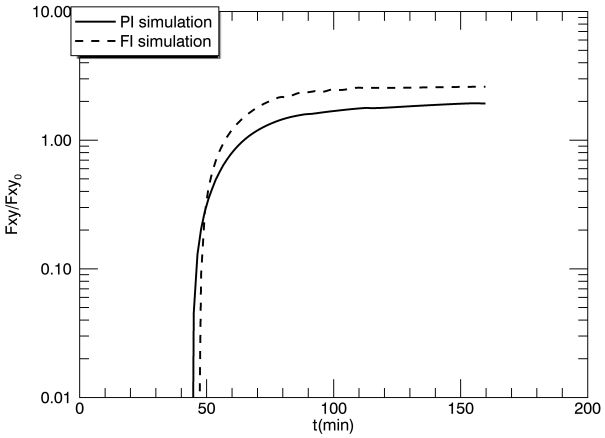

Figure 11. Emerged vertical in plane flux at z=1.2Mm.

Figure 12 shows the time evolution of E_{axial}. We find that the values of E_{axial} are higher (overall) in the PI case. This is mainly due to the initial conditions, where the subphotospheric field in both cases have the same plasma beta, but higher values for B and By in the PI case. We have performed one more simulation where the FI case has the same values for B and By with the PI case. In this third simulation, we find (not shown in this plot) that the E_{axial} starts to increase earlier and it reaches higher values, at least at the first local maximum of its time evolution. In all cases, the first peak corresponds to the initial emergence and expansion into the solar atmosphere. The oscillations after the first peak correspond to the eruptions of newly formed flux ropes due to the shearing along the PIL of the emerging bipolar regions.

3.4. *Magnetic flux emergence at solar atmosphere*

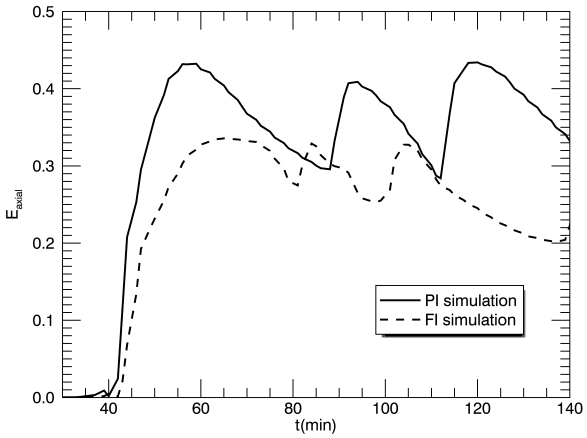

Figure 12. Time evolution of E_{axial} from $z > 0.36Mm$.

Figure 13 shows the emergence of the magnetic flux into the solar atmosphere, in the two experiments (FI and PI cases) with the same initial plasma beta for the sub-photospheric magnetic field. We have chosen two different times (t=3042s for the FI case and t=2782s for the PI case), when the apex of expanding volume has reached the same atmospheric height.

By looking at the magnetic field (B and By), we find that in the FI case, the emerging field experiences a more profound horizontal expansion. This is due to two main reasons: a) because the emerging field intersects the photosphere in a more vertical manner and b) the apex of the emerging field carries more dense plasma into the atmosphere in the FI case. Both reasons are side effects of partial ionization as we have discussed earlier.

The visualization of the temperature (collumn 2) confirms two results, which have been reported in previous numerical simulations Leake & Arber (2006). Firstly, the temperature inside the expanding field is lower than the background temperature due to the adiabatic expansion in the FI case. Secondly, in the PI case, the inclusion of the partial ionization reduces the adiabatic cooling. We have to highlight that this process does not heat the local plasma above nominal values. Therefore, perpendicular resistivity should be considered as a mechanism that reduces the heavy cooling from the adiabatic expansion, however it should not be considered (at least in this case) as a generic heating mechanism of the atmospheric plasma.

Figure 14 displays a quantitative measurement of the adiabatic cooling reduction due to the effect of partial ionization. We plot the temperature along height, at the center of the computational domain (x=y=0) for both cases, when the emerging field has expanded into corona. The temperature of the plasma inside the expanding volume increases to about 3000 K (solid black line), but it is still lower than the nominal background value (red solid/dashed lines).

In a similar manner to previous flux emergence simulations, we find that the emergence above the photosphere is followed by the formation of an erupting flux rope, due to the shearing and reconnection of magnetic fieldlines along the polarity inversion line. The eruption could be confined or ejective, depending on various parameters. Numerical experiments without ambient magnetic field in the solar atmosphere, (e.g., Fan 2001; Archontis & Török 2008; Archontis & Hood 2012), have shown that the eruptions can be confined when the downward tension of the outermost fieldlines of the emerging field can keep the flux rope within the expanding volume of the emerging field. This occurs when, e.g., the flux rope does not have enough free energy to push the outermost fieldlines strong enough and erupt in an ejective way. This could also occur when the numerical domain is small enough and the boundary conditions are closed, so that the expansion of the emerging field and the overall evolution of the magnetic system is limited. Some of these experiments have shown that the inclusion of a pre-existing magnetic field in the solar atmosphere, which can reconnect effectively with the emerging field, can lead to ejective eruptions of the flux ropes. Still, even with a pre-existing magnetic field, if the free energy of the flux rope is relatively small, the eruption is confined Leake et al. (2022). On the other hand, ejective eruptions can occur without reconnection between the emerging and the pre-existing magnetic field, (e.g., Fan 2009; Archontis et al. 2014; Syntelis et al. 2017). For instance, Syntelis et al. (2017) showed that successive eruptions can occur due to the combination of the torus instability and a tether-cutting reconnection of the fieldlines enclosing the flux rope. Our simulations have exactly the same initial conditions as the experiments by Syntelis et al. (2017) and, thus, the eruption mechanism (at least for the FI case) is the same. Figure 15 shows the first eruption of the FI case at $t = 82.56$ minutes (first row) and $t = 86.90$ minutes (second row). At $t = 82.56$ min, the core of the flux rope is located around $x = 0$ Mm and $z = 25 - 30$ Mm. The plasma around the center of the flux rope is cool (top-left panel) and dense (top-right panel). Underneath the flux rope, there is a hot vertical column of plasma. This column consists of a bidirectional pair of reconnection jets, which originate at the low corona (around $z = 3$ Mm) and are formed due to tether-cutting reconnection of the fieldlines surrounding the flux rope. At this stage of the evolution, the eruption is already undergoing an ejective phase. At $t = 86.90$ min (bottom row), the eruptive flux rope has left the upper part of the numerical domain, leaving behind a growing post-flare loop (its peak is located around $x = 0$ Mm, $z = 10$ Mm) and an intricate combination of hot and cool plasma in the corona. The onset and evolution of the eruptions for the FI and PI cases, and the similarities and

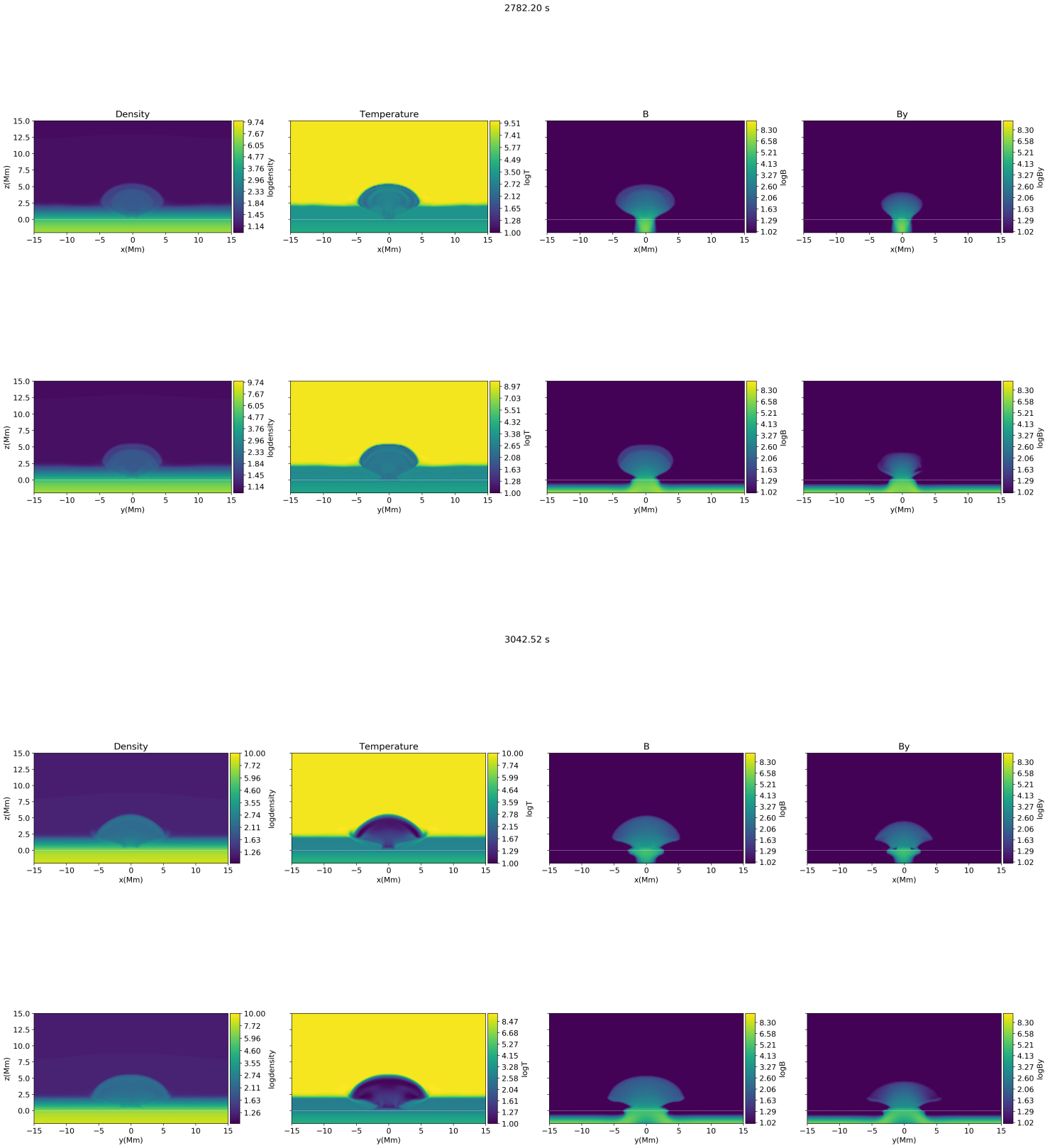

Figure 13. Visualization of various quantities (temperature, density, total magnetic field strength (B) and axial magnetic field (By)), for the PI case (first two rows) and the FI case (last two rows), at the vertical xz-midplane (rows 1 and 3) and at the vertical yz-midplane (rows 2 and 4), at two different times.

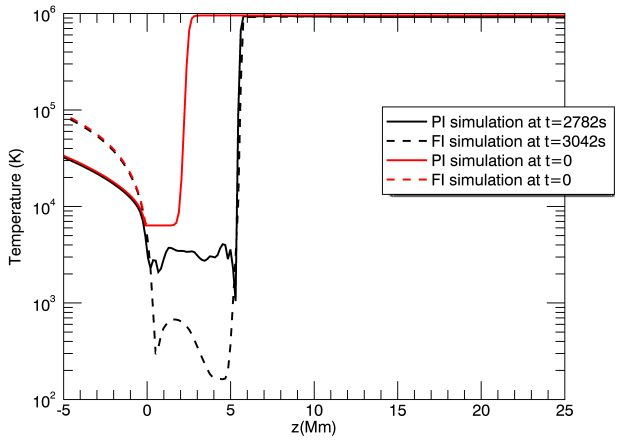

Figure 14. The comparison of the temperature profiles on both simulations in the x=y=0 plane in t=2782s on FI and t=3042s on PI.

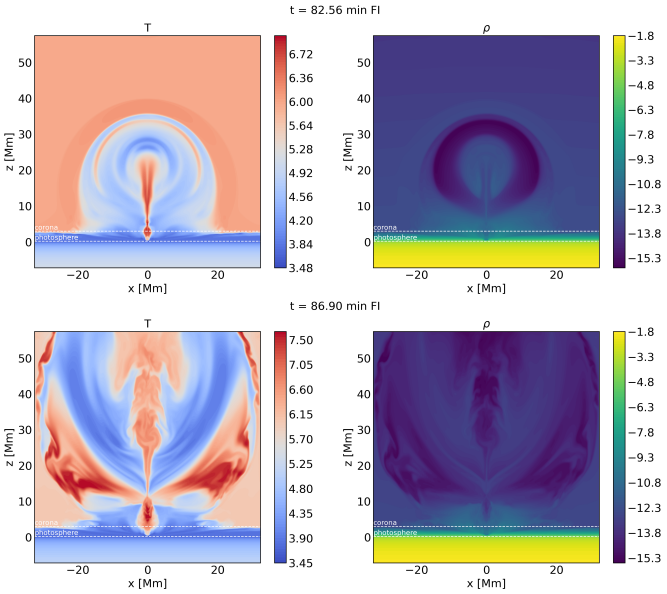

Figure 15. Visualization of the logarithm of the temperature and the logarithm of density in the xz midplane for FI simulation in t=82.56 minutes and t=86.90 minutes.

differences between the two cases, will be discussed in detail ina forthcoming paper.

4. CONCLUSIONS

We have performed 3-D numerical simulations to investigate the effect of partial ionization on the magnetic flux emergence process. We have modified the single-fluid MHD equations to include the effects of neutral hydrogen on our simulations. This modification induced a different induction equation which included the collisions between the three different species and how these collisions affect the evolution of the magnetic field.

We find that partial ionization affects the emergence of magnetic flux at the photosphere. The slippage effect is an imminent result of the ion-neutral collisions leading to the dynamic movement of the ions through the plasma and simultaneously the couple of neutrals to the magnetic field. This slippage explains the slow horizontal expansion and the spindle-like shape of the emerging structure of the magnetic field.

Another result of the aforementioned phenomenon is the failed emergence of the FT axis in the photosphere. More precisely, the apex of the FT experiences the slippage effect which takes place if the ion-neutral collisions are sufficient to decouple the ions from the field. The axis on the other hand still "experiences" ion-neutral collisions but they are not sufficient in order to decouple the ions so the collisions there act like a deceleration device leading to the failed emergence of the axis to the solar surface.

The ion-neutral collisions are also responsible for the less plasma that the PI axis is transferring to the solar atmosphere. This specific characteristic is the reason that the PI's apex starts to ascend towards the solar corona earlier than the FI case, although the emerging tubes in the two cases have the same plasma beta.

Since our numerical simulations are fully three-dimensional, we have studied also the appearance of the emerging field around the PIL at the photosphere. We have found that in the PI case, the polarities adopt a more circular-like shape. This is because the dominant magnetic field component in this case is the vertical component, Bz. On the other hand, the magnetic tails are more apparent in the FI case, where the azimuthal component of the magnetic field is very strong.

Previous studies (e.g. Khomenko & Collados 2012; Martínez-Sykora et al. 2015; Leake & Arber 2006; Leake & Linton 2013) have indicated that partial ionization due to the induced perpendicular resistivity could be an important heating mechanism in the solar atmosphere. However, our simulation show that the inclusion of PI could reduce the intensive cooling from the adiabatic expansion, yet it does not heat the plasma above the nominal background values.

We have also found that the amount of the emerged flux into the solar atmosphere is a little bigger in the PI simulation. However, this is mainly due to the fact that the initial sub-photospheric magnetic fields have the same plasma beta in both cases, but the initial field strength is bigger in the PI simulation. Therefore, the inclusion of PI can not determine (alone) the amount of flux transfer at and above the solar surface. Finally, our numerical experiments show that PI does not halt the formation of unstable structures at the PIL of the emerging region, which can eventually erupt into the outer solar atmosphere. To some extent, this result contradicts the

assumption, based on the outcome of previous 2.5D studies (e.g., Leake & Linton 2013), that PI may not help the creation of unstable coronal structures. The effect of PI on the recurrent eruptions and the comparison with the FI simulations, will be presented in a forthcoming study.

ACKNOWLEDGEMENTS

The authors acknowledge support from the Royal Society grant RGF/EA/180232. This work was also supported from the ERC synergy grant "The Whole Sun". The authors express appreciation to Dr. D. Nóbrega-Siverio and Professor F. Moreno-Insertis. Their contributions, during the ERC Synergy Grant workshop, "The Whole Sun", held at Paris-Saclay, provided helpful insights for our research. The work was supported by the High Performance Computing facilities of the University of St. Andrews "Kennedy".

REFERENCES

Arber, T., Longbottom, A., Gerrard, C., & Milne, A. 2001, Journal of Computational Physics, 171, 151 , doi: 10.1006/jcph.2001.6780

Arber, T. D., Haynes, M., & Leake, J. E. 2007, ApJ, 666, 541, doi: 10.1086/520046

Archontis, V., & Hood, A. W. 2012, A&A, 537, A62, doi: 10.1051/0004-6361/201116956

Archontis, V., Hood, A. W., & Tsinganos, K. 2014, ApJL, 786, L21, doi: 10.1088/2041-8205/786/2/L21

Archontis, V., Moreno-Insertis, F., Galsgaard, K., Hood, A., & O'Shea, E. 2004, A&A, 426, 1047, doi: 10.1051/0004-6361:20035934

Archontis, V., & Török, T. 2008, A&A, 492, L35, doi: 10.1051/0004-6361:200811131

Avrett, E. H., & Loeser, R. 2008, The Astrophysical Journal Supplement Series, 175, 229, doi: 10.1086/523671

Braginskii, S. I. 1965, Reviews of Plasma Physics, 1, 205

Brown, J. C. 1973, SoPh, 29, 421, doi: 10.1007/BF00150822

Fan, Y. 2001, ApJL, 554, L111, doi: 10.1086/320935

—. 2009, ApJ, 697, 1529, doi: 10.1088/0004-637X/697/2/1529

Khomenko, E., & Collados, M. 2012, ApJ, 747, 87, doi: 10.1088/0004-637X/747/2/87

Leake, J. E., & Arber, T. D. 2006, A&A, 450, 805, doi: 10.1051/0004-6361:20054099

Leake, J. E., Arber, T. D., & Khodachenko, M. L. 2005, A&A, 442, 1091, doi: 10.1051/0004-6361:20053427

Leake, J. E., & Linton, M. G. 2013, ApJ, 764, 54, doi: 10.1088/0004-637X/764/1/54

Leake, J. E., Linton, M. G., & Antiochos, S. K. 2022, ApJ, 934, 10, doi: 10.3847/1538-4357/ac74b7

Leake, J. E., Linton, M. G., & Török, T. 2013, ApJ, 778, 99, doi: 10.1088/0004-637X/778/2/99

Magara, T., & Longcope, D. W. 2001, ApJL, 559, L55, doi: 10.1086/323635

Manchester, IV, W., Gombosi, T., DeZeeuw, D., & Fan, Y. 2004, ApJ, 610, 588, doi: 10.1086/421516

Martínez-Sykora, J., De Pontieu, B., & Hansteen, V. 2012, ApJ, 753, 161, doi: 10.1088/0004-637X/753/2/161

Martínez-Sykora, J., Moreno-Insertis, F., & Cheung, M. C. M. 2015, ApJ, 814, 2, doi: 10.1088/0004-637X/814/1/2

Moreno-Insertis, F., & Emonet, T. 1996, ApJL, 472, L53, doi: 10.1086/310360

Moreno-Insertis, F., Galsgaard, K., & Ugarte-Urra, I. 2008, ApJL, 673, L211, doi: 10.1086/527560

Murray, M. J., Hood, A. W., Moreno-Insertis, F., Galsgaard, K., & Archontis, V. 2006, A&A, 460, 909, doi: 10.1051/0004-6361:20065950

Saha, M. N. 1921, Proceedings of the Royal Society of London Series A, 99, 135, doi: 10.1098/rspa.1921.0029

Syntelis, P., Archontis, V., Gontikakis, C., & Tsinganos, K. 2015, A&A, 584, A10, doi: 10.1051/0004-6361/201423781

Syntelis, P., Archontis, V., & Tsinganos, K. 2017, ApJ, 850, 95, doi: 10.3847/1538-4357/aa9612

Toriumi, S., & Yokoyama, T. 2011, ApJ, 735, 126, doi: 10.1088/0004-637X/735/2/126